Journal of Building Engineering 86 (2024) 108873

Contents lists available at ScienceDirect

Journal of Building Engineering

journal homepage: www.elsevier.com/locate/jobe

Bond-slip behaviour of textile-reinforcement in 3D printed concrete

Akilesh Ramesh, Pathmanathan Rajeev *, Jay Sanjayan

Centre for Sustainable Infrastructure and Digital Construction, Swinburne University of Technology, Australia

ARTICLE INFO

Keywords:
Rheology
High-performance concrete
Pull-out
Bond strength
Buildability
Pumpability

ABSTRACT

Integration of reinforcement in extrusion-based 3D concrete printing (3DCP) is one of the significant challenges that limit its structural application. Providing textile reinforcement having high tensile strength, easy formability and non-corrosive nature as a potential reinforcement for 3DCP members enhances their structural performance. However, the bond between the printed concrete and the textile reinforcement is an essential factor that affects the composite action. This study investigates the bond-slip behaviour of three types of textile reinforcements (i.e., AR-glass, basalt and carbon) in high-performance 3D printable concrete. The bond characteristics were evaluated using pull-out load test specimens. The effect of rheological properties like viscosity and yield strength on the bond behaviour was evaluated by varying the cement content with two different replacement dosages of fly ash and slag. The modification of the nozzle to incorporate textile reinforcement as an in-process reinforcement method for 3DCP is also discussed. Test results showed that the addition of fly ash reduced the viscosity and yield strength, thereby enhancing the bond strength and pull-out load. However, reduced viscosity and yield strength resulted in poor buildability. When compared to the control mix, the mix with 15% slag replacement showed 40% increased bond strength with good buildability and easy pumping. The modified nozzle incorporates the textile reinforcement during printing, and scanning electron microscopy images show that the printable concrete was observed to bond well with the multifilament yarns of the textile. Furthermore, analytical modelling was conducted to predict the pull-out load versus slip behaviour, and a comparison of the predicted and experimental behaviour is presented.

1. Introduction

Extrusion-based 3D concrete printing (3DCP) is an emerging automated construction technology that involves the deposition of concrete in a layer-by-layer manner to create freeform structures [1–3]. This technique allows architects to design complex geometrical shapes for structural members, which would be challenging to achieve using conventional construction methods, thereby providing greater design flexibility [4,5]. Despite its advantages, the broad implementation of this technology is primarily impeded by the challenge of developing printable materials with high strength and providing effective reinforcement techniques to enhance structural performance [6,7].

The printability of a 3D concrete mixture is primarily regulated by its rheological parameters, characterized by low initial viscosity and yield strength for ease of pumping, and a subsequent increase in static yield strength development to enhance buildability [8–10].

* Corresponding author.
E-mail addresses: aramesh@swin.edu.au (A. Ramesh), prajeev@swin.edu.au (P. Rajeev), jsanjayan@swin.edu.au (J. Sanjayan).

https://doi.org/10.1016/j.jobe.2024.108873
Received 8 January 2024; Received in revised form 14 February 2024; Accepted 18 February 2024
Available online 20 February 2024
2352-7102/

Additionally, concrete is classified as a non-Newtonian fluid, whereby it exhibits solid-like behaviour under low shear rates and liquid-like behaviour under high shear rates. These properties are influenced by the viscosity and yield strength of the mixture [11]. Furthermore, with time, the yield strength and viscosity of the concrete mix increase, conflicting with the requirements for printing and creating the need for establishing a critical period for the printing process. Previous studies have assessed various approaches for controlling the viscosity and yield strength of the printable mix. To improve the pumpability of the printable mix during printing, vibration around the extruder can be applied to reduce the yield strength and, consequently, the extrusion pressure [12]. Additionally, active rheology control methods have been developed by introducing accelerators or modifying the print head to provide accelerators at the nozzle head. These methods enhance the yield strength of the printable mix while maintaining its flowability for easy pumping [13,14]. Furthermore, previous studies have evaluated a secondary mixing method involving the addition of viscosity-modifying agents and recycled coarse aggregates as an onsite approach to improve the printability and buildability of ready-mix concrete [15].

The mechanical properties of 3D printable concrete are an essential parameter for structural applications, similar to its rheological parameters. However, like conventional concrete, 3D-printed concrete elements are strong in compression but weak in tension. The layer-by-layer deposition process creates weaker interface zones that affect the tensile load-carrying capacity of the element under tensile loading [16]. Reinforcing 3D printed structures presents challenges that require special strategies to avoid obstruction during the printing process. However, various reinforcing strategies have been developed, including the use of short fibres (such as glass, carbon, and steel), cable reinforcement, steel mesh, and steel bars [17–21]. Incorporating short fibres into 3D printable concrete during the mixing stage can improve flexural strength [22–24], and the fibres tend to align along the printing direction, resulting in fibre bridging along the printing path but not across the interlayers [25]. This limits the reinforcement between printed layers while vertical printing for wall, column and curvilinear façade elements. Furthermore, short fibres provides discontinuous reinforcing effect which reduces the composite action of 3D-printed structures. Conversely, providing mesh reinforcement improves the reinforcing effect in both directions along with a continuous reinforcement effect for 3D-printed structures improving the composite action [21]. However, due to the higher rigidity of steel mesh limits the printing of complex geometrical shapes [26]. Additionally, the layer-by-layer deposition process creates highly permeable interlayer zones that can affect the durability of 3D-printed structures [27]. Thus, providing conventional reinforcement for 3DCP structures requires to provide higher concrete cover resulting in thicker sections. Based on the research works so far, it can be said that effectively reinforcing complex curvilinear 3D printed elements using a continuous tensile system still remains a major challenge. To contribute to solving this challenge, this study proposes the use of textile reinforcement as a potential reinforcing method for 3D printing.

Over the past two decades, textile-reinforced concrete (TRC) has gained attention as a potential material for use as tensile reinforcement in concrete elements. Textiles possess desirable characteristics, such as a non-corrosive nature and easy formability, which enable the creation of curvilinear structures with slender cross-sections and complex shapes [28]. In comparison to short fibres, the continuity of textile yarns demonstrates higher first crack strength in the elastic stage under tensile stresses [29,30]. Comparison on the cyclic axial loading behaviour of fibre-reinforced and textile-reinforced columns showed that textile reinforcement improved the confining effect and thus enhanced the energy dissipation capacity and strength [31]. Furthermore, polymer coated textile reinforcement enhanced the flexural capacity under both static and impact loading when compared to steel fibre reinforced concrete beams [32]. In a study by Volkova et al. the flexural performance of TRC reinforced with carbon and AR glass textiles showed a higher residual load-carrying capacity when compared to unreinforced concrete [33]. Further, the composite action of a TRC element is mainly characterized by the bond between the textile and the cementitious matrix. Various techniques to improve bonding have been studied, among which epoxy-coated and prestressed textiles showed higher bond strength, regardless of the type of textile used [34]. Similarly, among the different fabrication processes for manufacturing TRC panels, the pultrusion process enhanced the bond between the textile and concrete due to a higher impregnation of concrete into the textile [35]. Hence, the bond between textile reinforcement and the 3D printed concrete needs detailed investigation to understand the composite action.

The rheological properties of the printable mix affect the bond between the textile and the matrix. Hence, the effect of viscosity and yield strength on the bond behaviour needs detailed evaluation. The analysis of interfacial bond behaviour between textile reinforcement and 3D-printable concrete mix results in better understanding of the composite behaviour. This results in adopting textile-reinforced 3D-printed concrete members in load bearing walls, roof structures, permanent formwork elements for columns and façade systems with enhanced structural performance and aesthetically pleasing geometrical shapes. In this study, the effect of rheology on the bond behaviour is evaluated by varying the cement content of the printable mix with two different replacement percentages of fly ash and slag. The addition of supplementary cementitious materials showed improved rheological characteristics with better mechanical performance [36,37]. The effect of fly ash and slag on the rheological properties was evaluated by measuring the viscosity, dynamic yield strength and static yield strength development using a rotational rheometer. The bond behaviour was evaluated by pull-out test on three different textiles (AR-glass, basalt and carbon). Incorporation of the textile as an in-process reinforcing method for 3DCP was carried out using the modified nozzle. Further, the effectiveness of the nozzle in bonding and the details of the printable concrete bonded to the multifilament yarns of the textile reinforcements were evaluated using scanning electron microscopy (SEM) micrographs. In addition, the pullout load vs slip behaviour was also formulated using analytical equations and was compared with the experimental results. Based on the comparisons, modifying the parameters to improve the model was also discussed for different mix proportions and textile reinforcements.

2. Materials and mix preparation

2.1. Concrete

Materials used for the preparation of the high-performance printable concrete mixes used in this study consist of Ordinary Portland cement (OPC) complying with AS 3972 [38] and silica fume, fly ash and slag complying with AS 3582.3 [39]. Sieve-graded silica sands with three different mean particle sizes of 879 μm (coarse sand), 460 μm (medium sand) and 224 μm (fine sand) were used as aggregates. The particle size distribution of binders and sands is shown in Fig. 1. In addition, a polycarboxylate ether-based superplasticiser (SP) and nano clay (a highly purified hydrous magnesium aluminosilicate) were used to tailor the workability and viscosity of the mixes respectively. Both the additives used are confirming to AS 1478.1 standards [40]. The properties of nano clay are provided in Table 1.

2.2. Textile reinforcement

Three different commercially available textile reinforcements, namely AR-glass, Basalt and Carbon textile, as shown in Fig. 2 were used in this study to evaluate the bond behaviour between the reinforcement and 3D printable mixes. The textiles are made up of multifilament yarns in both perpendicular directions and are shown in Fig. 2. The main reinforcing direction of the textiles is along the longitudinal direction and is represented as "warp" in Fig. 2. Similarly, the transverse yarns denoted as "weft" in Fig. 2 hold the warp yarns together and provide continuity to the textile. The reinforcing yarns in both the direction are not having any type of additional coating or impregnation. The physical properties of the textiles are given in Table 2. The tensile strength of the warp yarns given in Table 2 represents the strength of five yarns tested under tension and the strength is represented in N/50 mm.

2.3. Mix preparation

The mixing was carried out in a planetary mixer by adding all the dry materials to the mixing bowl. Slow mixing was performed for about 2 min to achieve a homogeneous mixing of the materials. Later, three-quarter of the water was mixed with superplasticiser and added slowly and continued mixing at a slow speed for another 5 min. Afterwards, the remaining water was added and mixed for an additional 3 min. Finally, nano clay was added to the mixture and mixed for 5 min at high speed. The details of the mix proportion adopted for the printable mixes in this study are given in Table 3. It is to be noted that, adding fly ash and slag as a replacement for OPC not only affects the rheological properties but also reduces the carbon footprint. Further, the replacement of fly ash and slag was limited to 30 % as further increase resulted in increased flow which adversely affects the printability of the mix and also can reduce the mechanical properties [24]. However, in all the mixes the silica fume content was kept at 30 % as this was observed to be the optimum dosage for improving the mechanical strength in high-performance mixes [41].

3. Experimental program

3.1. Nozzle modification

Unlike the various reinforcement strategies adopted previously for 3D concrete printing, an in-process reinforcement method is used in this study. The textile reinforcement is placed along with the concrete printing process with a modified print nozzle. A similar strategy was adopted in previous studies by designing a nozzle with a vertical slit in the middle to accommodate the steel mesh reinforcement while printing [21]. Further, the textile reinforcement strips placed using the modified nozzle are not connected firmly and are held together by the bond between the textile and the concrete matrix. The details of developing the modified nozzle are shown in Fig. 3.

Printable concrete has a higher viscosity and static yield strength development when compared to conventional concrete [9]. Hence, increasing the nozzle length results in increased extrusion pressure and higher energy requirements. Thus, considering the limiting extrusion pressure of the gantry 3D printer, the nozzle length was increased to adopt a textile reinforcement strip of 100 mm, which measures ten times the layer thickness (a printed concrete layer thickness of 10 mm is used in this study). Increasing the nozzle length even with a gradually varied slope resulted in de-bonded printing as shown in Fig. 3(a). Hence, while gradually increasing the

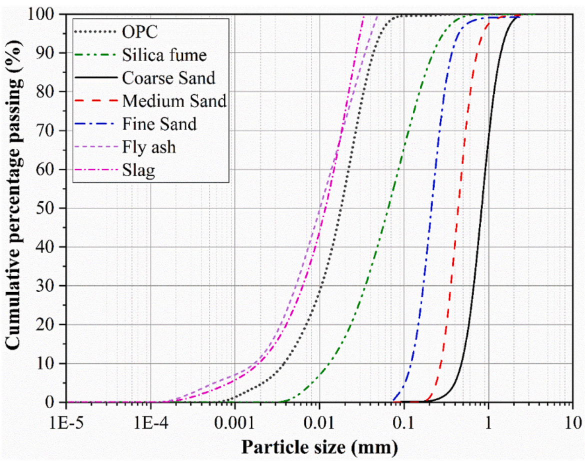

Fig. 1. Particle size distribution for all dry materials.

Table 1
Properties of nano clay (provided by the supplier).

pH	Specific gravity	Water solubility (Cl^{-1})	Acid solubility (Cl^{-1})
8.5 – 9.3	2.29	<0.001	0.007

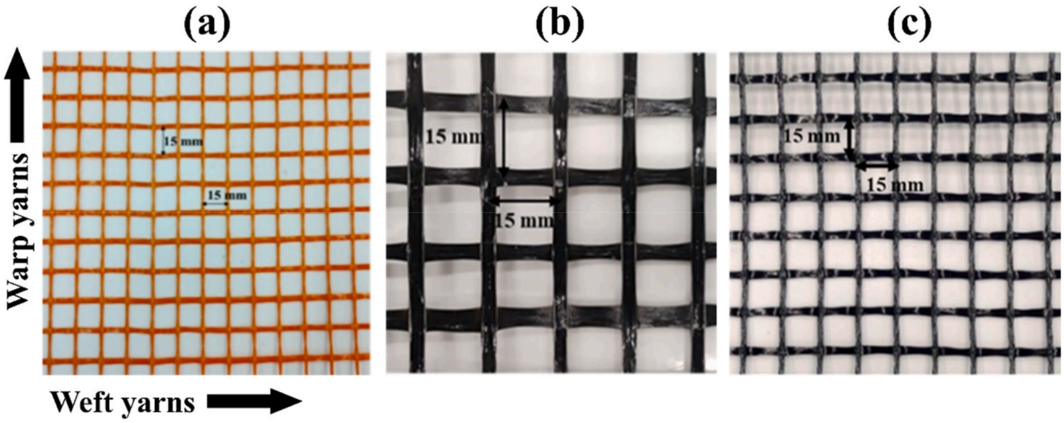

Fig. 2. Textile reinforcement (a) AR-glass; (b) Basalt; (c) Carbon textile.

slope through the nozzle length, an additional curvature was provided at the end which allows an inward flow of the concrete mix. However, a vortex created at the end by a sudden change in the flow path resulted in an increased flow and the printed concrete layer's surface quality and layer thickness were observed to be non-uniform as shown in Fig. 3(b). To control the outflow of the concrete at the end of the nozzle, the opening size was reduced and streamlined in such a way that the concrete flows in towards the textile and creates uniformly printed layers as shown in Fig. 3(c).

3.2. 3D printing process

Fig. 4(a) shows the gantry type 3D printer used in this study for printing the pull-out test specimens. The printer has a gantry system that provides the movement of the auger type extruder as shown in Fig. 4(b) along the printing platform having a space of 1.8 m × 1.6 m × 1.8 m. A customised computer program is used to monitor the X, Y and Z directional movement of the printer. The program consists of a G-code developed to print the required shape and consists of the X and Y co-ordinates of the desired shape to be print. The concrete mix was added to the extruder with the help of a feeder mounted to the extruder. The printer was controlled to move at 20 mm/s along the X and Y direction and was programmed to move 10 mm in the Z direction after the completion of each layer. The modified nozzle is attached at the end of the extruder to deposit the printable mix along the path.

The textile reinforcement was placed on the print bed and held at one end. The modified nozzle move over the placed textile aligning it along the print path. The extruded concrete through the nozzle encases the textile reinforcement along the printing process. Further, textile can easily align along the printing path and the encased concrete holds the reinforcement in position. It is to be noted that textile reinforcement was not provided with any additional coatings or impregnation. To prepare the pull-out specimens, 400 ± 2 mm long specimens with two 30 ± 2 mm wide layers of concrete (forming a total thickness of 20 ± 2 mm), encasing the textile reinforcement were printed for all three types of textiles as shown in Fig. 4(c). The specimen width and concrete flow were adjusted by controlling the extrusion rate by regulating the auger's rotational speed. The printable mixes surface quality was evaluated by visual inspection and was observed to have a smooth and unform printed surface. The printed specimens were covered for 24 h to avoid moisture loss and then were immersed in water and kept in an oven for 48 h at 90 °C for steam curing. However, care was taken to avoid any damage to the textile during steam curing. Later, the specimens taken from the oven were kept at room temperature (23 ± 3 °C) for another 72 h.

3.3. Rheological properties

To measure the rheological properties of the concrete mixes, the researchers used a rotational rheometer called Viskomat XL [42]. The rheometer vessel, with a diameter of 135 mm and a height of 170 mm, was filled with fresh concrete, and a six-blade vane with a height of 69 mm and a radius of 34.5 mm was immersed into it. The vessel was rotated to apply the shearing protocol while the vane remained still, and the torque was measured. The extended Reiner-Riwlin equation was used to obtain the shear stress, shear rate, and viscosity based on the torque and rpm [43]. A steel cage was used to prevent the concrete from slipping off the inner face of the vessel. Additionally, the mixes were visually inspected during the process to avoid errors in plug flow and confirmed that there were no plug cavities. The measurements were repeated three times for each mix, and the average results were reported to ensure the homogeneity of the data and avoid anomalies.

Table 2
Properties of the textile reinforcement[a].

Textile	Weight (g/m^2)	Area of warp yarns per 100 mm width (mm^2)	Tensile strength of five warp yarns (N/50 mm)	Linear warp yarn density (tex)	Modulus of elasticity (GPa)	Equivalent diameter of warp yarn (mm)
AR glass	335	12.37	3100	2560	72	1.5
Basalt	238	13.88	2700	1800	80	1.6
Carbon	408	12.37	4950	1600	215	1.5

NOTE: Mesh sizes of all three textiles are 15 mm x 15 mm.
[a] Provided by the supplier KAST GmbH, Germany.

Table 3
Mix proportion.

Mix ID	OPC	Silica fume	Fly ash	Slag	Fine sand	Medium sand	Coarse sand	Water binder ratio	SP[a] (%)	Nano clay[a] (%)
C-0F-0S	0.7	0.3	0	0	0.4	0.3	0.3	0.16	1.0	0.25
C-15F-0S	0.595		0.105	0						
C-30F-0S	0.49		0.21	0						
C-0F-15S	0.595		0	0.105						
C-0F-30S	0.49		0	0.21						
C-15F-15S	0.49		0.105	0.105						

Note: Mix ID represents the following, C, F, and S stand for control mix, fly ash and slag, respectively. The mix C-0F-15S represents a control mix with no fly ash and 15% cement replacement by slag.
[a] Superplasticizers and nano clay are % by weight of the binders.

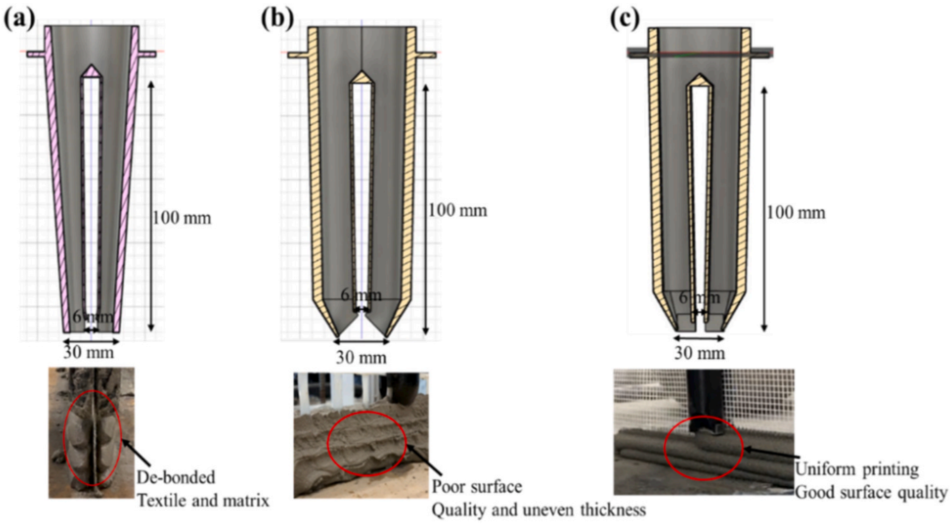

Fig. 3. Modified nozzle (a) Length modified; (b) Providing convergence at the end; (c) Streamlining the flow at the end.

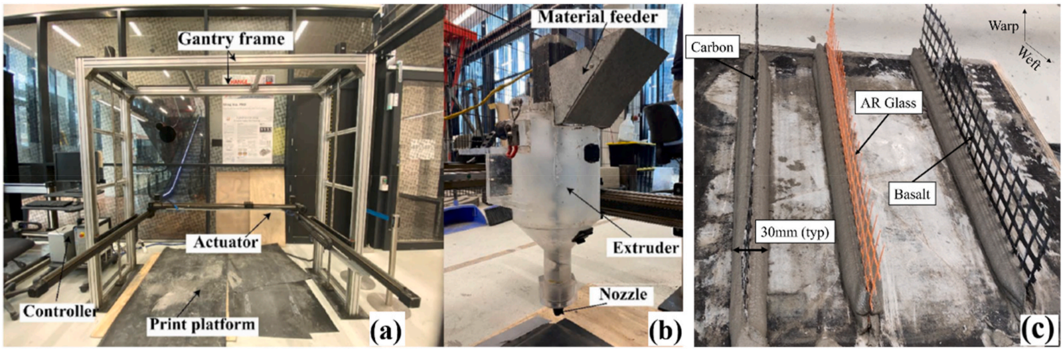

Fig. 4. (a) Gantry type 3D printer; (b) Auger type extruder [9]; (c) 3D printed specimens with three different textiles for pull-out test.

3.3.1. Apparent viscosity and dynamic yield strength

The effect of fly ash and slag on printable concrete mix rheological properties was evaluated in terms of changes in the mix viscosity and dynamic yield strength. Mix's apparent viscosity and dynamic yield strength were derived from the flow curve. The shearing behaviour similar to previous studies of the authors [42] was adopted to obtain the flow curve for all the mixes. The mixes were pre-sheared to avoid any transfer period differences. The maximum shearing rate of 6.45 s^{-1} was achieved in increments of 0.8065 s^{-1}, which were retained for 30 s to reach a constant state. The total flow curve took approximately 7.5 min. The average shear stress calculated corresponding to the last 5 s of each step was used as the shear stress at that shear rate. The downward section of the flow curve was used to calculate the apparent viscosity and dynamic yield strength of fresh concrete [42,44].

3.3.2. Static yield strength development over time

The buildability of the mix is a critical factor that impacts the performance of 3D concrete printing. Therefore, it is essential to evaluate the effect of the addition of fly ash and slag to the mix on the variation in the buildability. Typically, the fresh concrete mix may fail due to material failure, which is caused by plastic yielding, or due to stability failure, resulting in buckling failure and is associated with the concrete stiffness [45,46]. To prevent material failure, the stresses induced by the gravity force of the subsequent layers must be resisted with the static yield strength of the concrete mix. Thus, the penetrometer test was used in this study to measure the static yield strength development over time to investigate the material failure. The static yield strength of the concrete is measured based on the load resistance during penetration of the mix using a penetrometer needle [13,14]. Fig. 5 shows the penetrometer test setup used in this study. The static yield strength of the concrete is measured based on Equation (1) [47].

$$\tau_o = \frac{F}{\pi R\sqrt{R^2 + h^2}} \tag{1}$$

where F is the resisted force in N *and* R and h represents the radius and height of the needle cone in mm, respectively. Three tests were performed for each mix, and the loading rate was maintained at 0.166 mm/min, with the test conducted for 30 min for each mix.

3.4. Pull-out bond test

The specimens printed as shown in Fig. 4 were saw-cut for preparing specimens for pull-out tests after the curing period. For each type of textile and mix proportion, six specimens were prepared with 40 ± 2 mm length, 30 ± 2 mm width, and 20 ± 2 mm height. The textile projected 75 mm from the printed layers, which constitutes a gripping length of 50 mm and a free length of 25 mm (to account for the variations from the initial elongation of the textile under applied tensile loading) [35]. The embedded length of the textile reinforcement was the same as the height of the printed layers (two 10 mm layers forming a total of 20 ± 2 mm) and was kept constant for all the specimens. The thickness of the printed concrete layer is fixed and controlled by the program guiding the print path which is transferred to the printer. As a result, a consistent layer thickness of 10 mm is maintained, ensuring embedded length of the textile to remain constant throughout the experiment. To assess the effect of the rheological properties of the mixes on the pull-out bond behaviour, only three warp yarns were simultaneously pulled together for each textile. Furthermore, in all the specimens two weft yarns were embedded in the concrete matrix. The textile reinforcement was oriented in such a way that the warp yarns are perpendicular to the printing direction. The pull-out test as shown in Fig. 6 was performed to measure the bond strength, pull-out energy and load-slip behaviour between the embedded textile and the printed mix for all the specimens. The test was conducted using an MTS machine which can apply a uniaxial tensile load at a constant displacement rate of 0.5 mm/min. The total elongation of the textile yarns were measured using the testing machine. The test was continued until the textile yarns exhibited complete slip from the 3D-printed concrete matrix, which is indicated by the lack of variation in the pull-out load. The bond strength between the textile and matrix was calculated by assuming a constant shearing along the embedded length due to friction and was calculated using Equation (2).

$$\tau = \frac{P_{max}}{n\pi dl} \tag{2}$$

where, $P_{\max}$ is the peak pull-out load, n is the number of warp yarns pulled together, d is the equivalent bundle diameter and l is the embedded length. To understand the difference in the impregnation of the printable concrete with each type of textile, SEM analysis was done for specimens of a selected mix proportion, before and after the pull-out test.

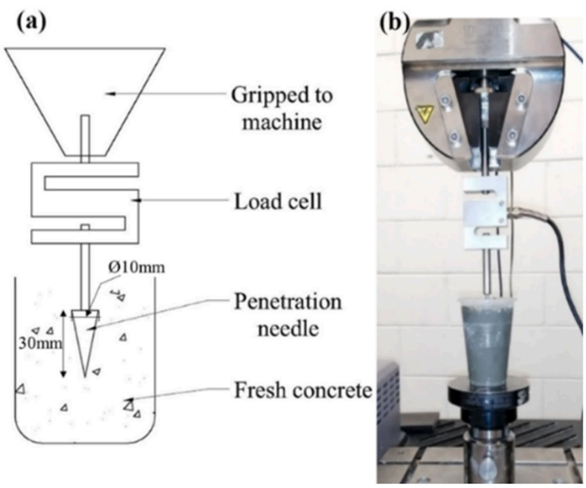

Fig. 5. Penetrometer test setup: (a) schematic diagram; (b) experiment setup [42].

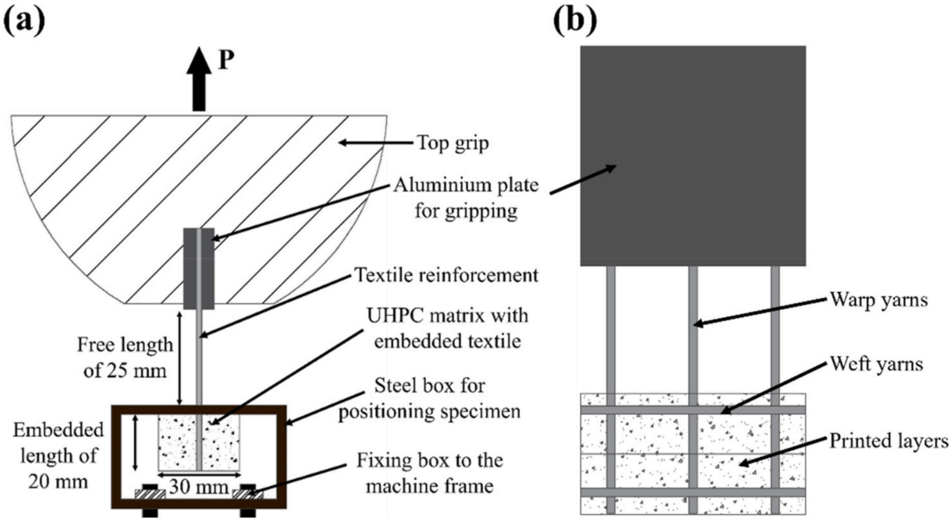

Fig. 6. (a) Schematic representation of the pull-out test setup (b) details of the pulled out yarns in the test specimen.

4. Results and discussion

4.1. Apparent viscosity and dynamic yield strength

3D printable concrete mixes have high viscosity and yield strength. The modified Bingham model is used to fit the flow curve as the model predicts the non-linear rheological behaviour of cementitious materials better [43,48]. The shear stress - shear rate curve for all the mixes fitted to the Modified Bingham model is shown in Fig. 7.

From Fig. 7, the effect of fly ash and slag on the variation in shear stress with increasing shear rate can be evaluated. The control 3D printable mix showed higher shear stress for all the shear rates. However, the addition of fly ash and slag reduced the shear stress of the printable mix. 30 % replacement with fly ash showed the lowest shear stress and can be attributed to the increase in flowability due to the spherical shape of fly ash [24,49]. Replacement with slag lowered the shear stress but was higher than the mixes with fly ash. This increase in shear stress when incorporating slag can be attributed to its higher water absorption capability, which is a consequence of the lower surface area of slag particles. The incorporation of both fly ash and slag as substitutes for cement in the printable control mix led to a reduction in shear stress when compared to the control mix. Higher shear stress necessitates for an increase in the extrusion pressure, impacting the printability of the mix and making it unfeasible. Consequently, the inclusion of fly ash and slag to the mix reduces the shear stress requirement of the printable mix, leading to a lower extrusion pressure and facilitates uniform printing. Furthermore, to understand the effect of fly ash and slag on the pumpability of the 3D printable mixes, the variation in the apparent viscosity and the dynamic yield strength were evaluated and represented in Fig. 8(a) and (b) respectively.

The apparent viscosity of all the mixes reduced with increasing shear rate, thus confirming that all the mixes showed a shear thinning behaviour. The addition of fly ash and slag reduced the viscosity of the mix at a lower shear rate when compared to the control mix indicating the ease in pumping. Reducing the viscosity of the printable mix improves its flowability and consequently enhance the

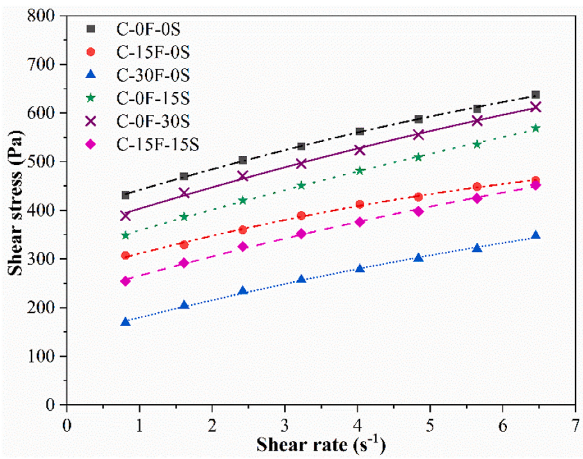

Fig. 7. Flow curve of the mixes fitted to the modified Bingham model.

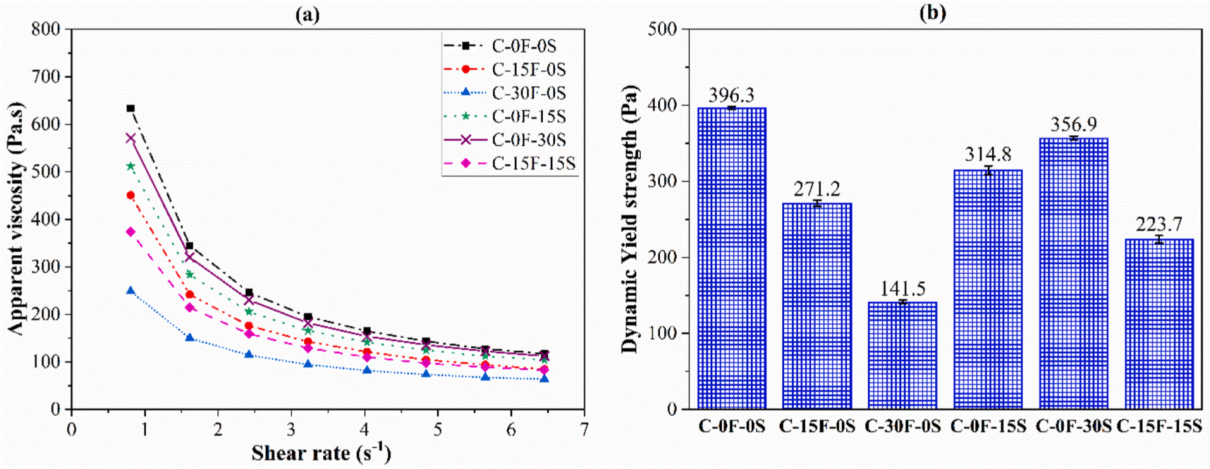

Fig. 8. (a) Apparent viscosity vs shear rate; (b) Dynamic yield strength (error bar indicates mean ± one standard deviation).

lubrication properties of the mix during the pumping process. This leads to a decrease in the pumping pressure and also mitigates the clogging issues of the printable mix. However, the addition of fly ash reduced the viscosity significantly. Furthermore, to characterise the pumpability, dynamic yield strength values should be less than 1300 Pa for a smooth pumping of the 3D printable mix [50]. The addition of fly ash reduced the yield strength with increased flowability whereas the replacement of slag increased the yield strength when compared to fly ash mixes.

4.2. Static yield strength development

Fig. 9 illustrates the static yield strength development over time for all the mixes in this study. The penetrometer test results up to 30 min from mixing was reported in this study as this period can be adopted as the crucial time during the printing process [8,14]. The static yield strength of 3D printable mixes increases with time due to the thixotropic nature of the printable mixes. The test was started after 3 min from the mixing to account for the transfer time during the actual printing process. Irrespective of the mix compositions, the 3D printable mixes showed a rapid increase in yield strength during the initial stage. Compared to the control mix, the addition of fly ash and slag reduced the static yield strength development. Moreover, the addition of fly ash resulted in reduced static yield strength development due to the high flowability of the fly ash mixes. Thus, the addition of fly ash reduces the buildability of the printable mix. Moreover, in order to assess the significance of the variation observed in the static yield strength development, a statistical analysis was performed using Welch's *t*-test. The *t*-test was used to compare the variations in all the mixes in relation to the control mix C-0F-0S. It was observed that, the mixes C-15F-0S, C-30F-0S and C-15F-15F exhibited a significant variation in the static yield strength development indicated by a lower p-value from the *t*-test compared to the assumed significance level of 0.05. However, the addition of slag showed a higher rate of increase in the static yield strength and the 30 % addition of slag showed comparable static yield strength development to the control mix. This was further substantiated by the static test, where the p-value was observed to be greater than the assumed significance level. Thus, the addition of slag resulted in no significant variation in the static yield strength development,

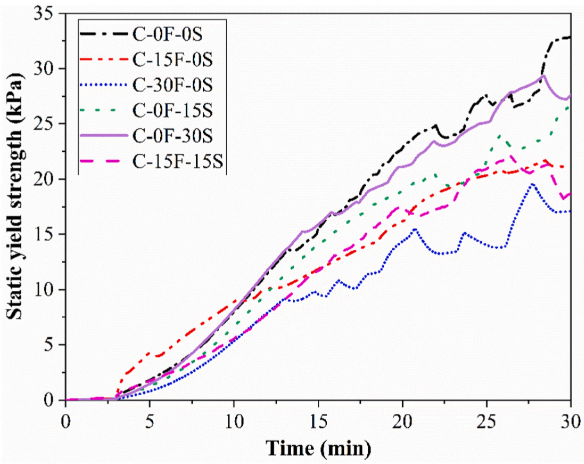

Fig. 9. Static yield strength development over time for all the mixes.

indicating that it does not adversely affect the buildability performance.

4.3. Pull-out bond behaviour

The pull-out load vs slip behaviour for all three textile types for different mix proportions are shown in Fig. 10. Irrespective of the type of textile and mix proportion, all the specimens showed similar pull-out behaviour without rupture of the textile yarns. Initially, an elastic stage was observed, and the textile elongates until the peak load. Further, a descending portion corresponding to the debonding phase (which represents the region in which the textile yarns start to slip from the concrete matrix after reaching the maximum bond strength) is followed. Finally, a steady flat region with no increase in the load was observed, which corresponds to the frictional slipping stage. However, the carbon textile showed a partial decrease in the pull-out load during the initial stage due to intermediate breaking of some of the filaments in the warp yarns for 15 % fly ash replaced mix and 15 % and 30 % slag replaced mix. This could be due to the higher modulus of elasticity of the carbon textile yarns when compared to the printable concrete resulting in higher shear stress transfer at the interface even from lower strains. It is important to note that during the pull-out testing, only the warp yarns were pulled out of the matrix and the weft yarns remained inside, similar behaviour was observed in other research [35]. Additionally, no cracks or damage were observed in the concrete matrix during the pull-out test, as the matrix is subjected to only compression. However, upon reaching the maximum bond strength, the textile exhibited debonding accompanied by minor interfacial cracking. It is to be noted that the textile mesh size and weave pattern of fibres have a significant effect on the bond behaviour [51,52]. However, current study adopts textiles with same mesh size and as a result the effect of mesh size was not evaluated. When compared to the control mix, 30 % fly ash replacement not only improved the peak load but also enhanced the elastic and debonding phases which results in improved toughness which is calculated as the area under the load vs slip curve until 2 mm slip. The increased toughness shows the enhanced energy dissipation capacity and a larger area in the first two phases represents enhanced composite action before complete debonding. The toughness indicating the bond performance and composite action was observed to be similar between the different mixes, however, carbon textile reinforcement showed higher toughness when compared to other type of textiles. Even though the 15 % fly ash replaced mix improved the flowability, pull-out load behaviour was observed to be similar to the control mix. However, the addition of slag improved the pull-out behaviour of the control mix and can be attributed to the enhanced bonding between the concrete and the textile due to improved penetration of the smaller-sized slag particles between the filaments. Further, when compared to fly ash replaced mixes, slag replaced mixes showed better stiffness for all basalt and carbon textile. The stiffness indicates the slope in the initial elastic phase and better stiffness results in better pull-out load capacity.

From the pull-out load behaviour, it can be observed that mixes with low viscosity and dynamic yield strength increase the pull-out load and improve the bond between the textile and the printable concrete. However, low viscosity results in poor buildability which is an important parameter during 3D concrete printing. Hence, a 3D concrete printable mix should have good buildability with sufficient ease in pumping while providing a better bond between textile and matrix to enhance the composite action during structural applications. Table 4 shows the summary of the results of the pull-out load test for all mix proportions and the three different textile reinforcement types. The bond-slip behaviour of 3D printable concrete and textile reinforcement is not quantitatively evaluated, however, some previous studies [53,54] have reported a better bond between printable mix and textile reinforcement. However, the bond behaviour of textile reinforcement and conventional concrete was observed to have similar pull-out behaviour. Moreover, depending on the textile type, embedment length and preparation method the bond strength and peak pull-out load varied. Nevertheless, a peak pull-out load exceeding 500 N was observed for the conventional preparation method, indicating that the bond strength observed in the current study is comparable [55,56]. From the results, it can be observed that carbon textile reinforcement showed the highest initial bond stiffness for all the mix proportions. It can be observed that the highest bond strength was observed for mixes with 30 % fly ash replacement. However, the C-30F-0S mix showed the lowest static yield strength development which results in low buildability and can be stated as not feasible for 3D concrete printing. Furthermore, the C-0F-15S mix showed good static yield strength development with comparably lower viscosity and dynamic yield strength for ease in pumping. The C-0F-15S mix showed 41 %, 25 % and 3 % improved bond strength for AR-glass, basalt and carbon textiles respectively when compared to the C-0F-0S mix. The toughness of the C-0F-15S mix was observed to be similar to the control mix. Whereas, the C-15F-15S mix showed improved bond

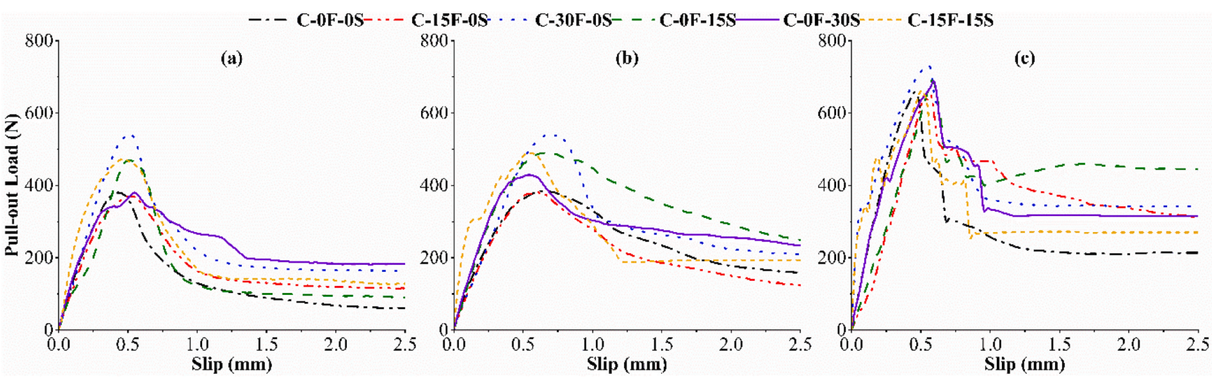

Fig. 10. Pull-out load vs slip behaviour (a) AR-glass; (b) Basalt; (c) Carbon.

Table 4
Pull-out test results summary (error bar indicates mean ± one standard deviation).

Textile reinforcement	Mix id	Maximum pull-out load (N)	Bond strength (N/mm^2)	Toughness (Nmm)	Slip at peak load (mm)
AR-glass	**C-0F-0S**	384.8 ± 3.9	1.14 ± 0.10	438.4 ± 89.6	0.53 ± 0.20
	C-15F-0S	378.2 ± 7.1	1.18 ± 0.02	383.0 ± 45.5	0.52 ± 0.10
	C-30F-0S	550.6 ± 7.9	1.87 ± 0.04	505.9 ± 84.2	0.53 ± 0.04
	C-0F-15S	491.9 ± 7.1	1.61 ± 0.02	407.4 ± 30.0	0.52 ± 0.04
	C-0F-30S	439.3 ± 16.1	1.40 ± 0.05	365.2 ± 33.9	0.63 ± 0.29
	C-15F-15S	477.9 ± 9.1	1.50 ± 0.03	447.9 ± 23.4	0.54 ± 0.09
Basalt	**C-0F-0S**	399.9 ± 8.9	1.76 ± 0.04	536.5 ± 46.9	0.71 ± 0.15
	C-15F-0S	384.9 ± 8.4	1.69 ± 0.04	460.2 ± 40.0	0.60 ± 0.05
	C-30F-0S	581.0 ± 12.4	2.57 ± 0.12	629.7 ± 157.6	0.73 ± 0.10
	C-0F-15S	511.0 ± 7.8	2.20 ± 0.03	683.1 ± 64.5	0.67 ± 0.12
	C-0F-30S	474.5 ± 11.0	2.01 ± 0.05	544.5 ± 23.8	0.52 ± 0.10
	C-15F-15S	494.8 ± 11.0	1.75 ± 0.03	505.6 ± 54.6	0.60 ± 0.05
Carbon	**C-0F-0S**	671.9 ± 10.7	2.58 ± 0.09	560.9 ± 55.6	0.47 ± 0.02
	C-15F-0S	692.4 ± 10.2	2.50 ± 0.04	581.4 ± 72.1	0.56 ± 0.02
	C-30F-0S	749.7 ± 14.9	2.76 ± 0.06	495.3 ± 95.9	0.57 ± 0.06
	C-0F-15S	711.0 ± 9.2	2.69 ± 0.08	718.8 ± 24.1	0.60 ± 0.02
	C-0F-30S	691.2 ± 7.4	2.65 ± 0.03	576.4 ± 13.5	0.61 ± 0.01
	C-15F-15S	697.8 ± 6.5	2.66 ± 0.02	456.0 ± 9.5	0.55 ± 0.04

strength when compared to the control mix, however, the static yield strength development was observed to be lower than the C-0F-15S mix. From the test results, it is evident that the bond between textile and matrix not only depends on the type of textile but also the rheological properties. Based on the rheological properties and the pull-out load behaviour, the replacement with 15 % slag was observed to show the best performance in both properties.

Fig. 11 shows the SEM micrographs for the three different textile reinforcements embedded in the C-0F-15S matrix before and after pull-out. It can be observed that the 3D printed matrix has penetrated between the filaments of the warp yarns which explains the good bonding observed between the textile and matrix. Further, this explains that the modified nozzle provides a better flow of the printable mix along and across the textile filaments resulting in good bonding. In addition, unlike the AR-glass textile, basalt and carbon textile yarns showed severe damage to the filaments after pull-out. The AR-glass textile after being pulled out, was observed to have concrete penetrated along the filaments which explains the highest bond strength enhancement when compared to basalt and carbon textile for the C-0F-15S mix.

5. Analytical prediction of pull-out bond-slip behaviour

The test setup adopted in this study results in a tensile force on the textile reinforcement and a compressive force on the 3D-printed

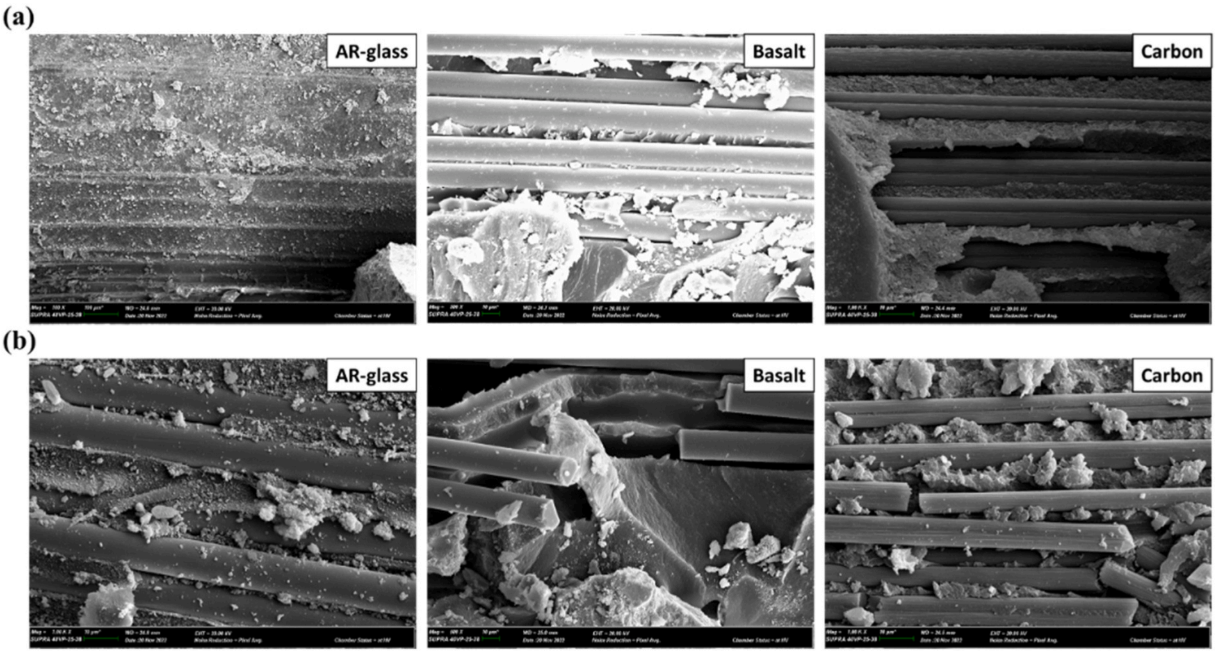

Fig. 11. SEM micrographs for all the textiles (a) before pull-out; (b) after pull-out (the images are to a scale of 10 μm).

concrete. Hence, the model developed in a previous study [57] was taken as the reference to predict the bond-slip behaviour of 3D-printed concrete and textile reinforcement. The beneficial effect of the transverse weft yarns of the textile is not taken into consideration to simplify the model. A typical pull-out behaviour consists of three stages as shown in Fig. 12(a) and the pullout force and deformation are formulated for each stage separately to predict the behaviour. The initial stage represents an elastic phase during which both the textile and the matrix resist the pull-out force util the peak bond strength is reached. Subsequently, the textile begins to debond from the matrix, displaying a non-linear pull-out behaviour throughout the second stage and continued till the textile is completely de-bonded. Finally, the textile undergoes a frictional slip marking the third stage. Similar pull-out behaviour was observed in previous studies, and the analytical model adopted in this study has also been employed to predict the pull-out behaviour [56,58,59]. The shear stress distribution will be linear till the maximum bond strength (τ_{max}) and then during the debonding stage, the stress will be controlled by the frictional bond strength (τ_{frc}). Further, when the textile is completely debonded from the concrete, sliding begins and the stress will be due to a constant dynamic bond strength (τ_{dyn}). The typical shear stress distribution during the pull-out test is shown in Fig. 12(b).

To satisfy the basic static equilibrium conditions along the embedded length of the textile, the pull-out force is transferred through the interface shear stress and the second order differential equation can be represented as in Equation (3).

$$\frac{d^2F}{dx^2} - \beta^2 F = 0 \tag{3}$$

where, $\beta^2 = \varphi\kappa Q$ and $Q = \left(\frac{1}{A_t E_t} + \frac{1}{A_c E_c}\right)$; φ is the circumference of the textile, κ is the slope of the linear portion of the shear stress vs slip diagram, A_t and A_c are the cross-sectional areas E_t and E_c are the modulus of elasticity of textile reinforcement and concrete respectively. From the differential equation, the pullout load vs slip behaviour for each stage is calculated and compared to the experimental results.

5.1. Functions to predict the pull-out behaviour

As observed from the experimental results, the pullout response showed three different stages. During the initial stage, the textile reinforcement can be assumed to be fully bonded and the slip shows a linear variation with the pull-out load till the maximum bond strength is reached. Hence, using the following Equation (4) the slip corresponding to an incremental load is calculated.

$$S_{stage1} = \frac{PQ'}{\beta \sinh(\beta L)}[\cosh(\beta L) - 1] \tag{4}$$

where, S_{stage1} is the slip in mm, P is the pull-out load in N, L is the embedded length in mm and $Q' = l_f \times \left(\frac{1}{A_t E_t} + \frac{1}{A_c E_c}\right)$, l_f is the free length of the textile provided in the pullout test. The slip observed in the experimental results is affected by the free fabric length [60] and from previous studies, the flexibility of the interface is proportional to the free fabric length [61]. Hence, to accommodate the effect of free length adopted in the experimental test, the correction was introduced to the inverse stiffness Q. Q' is defined here as the corrected inverse stiffness of the interface, or flexibility of the interface. This parameter is later modified for the experimental results. Hence the modified Q' was used in this study to evaluate the parameters, based on the equation, $Q_c = \alpha Q'$, where α is a correction factor, and Q_c is the modified inverse stiffness.

Further, as the load increases, the interface shear stress increases to the maximum bond strength and the limiting slip S_1 as shown in Fig. 12(b) is determined from the experimental bond strength vs slip diagram and is considered to mark the debonding stage 2. During the debonding stage, the textile reinforcement begins debonding over a length of d and remains bonded over the length $L - d$. The interface shear stress consists of a stress distribution due to a constant frictional bond strength (τ_{frc}) in MPa over the debonding region and stress due to the maximum bond strength (τ_{max}) in MPa over the remaining region. Thus, the pullout force and the slip during the second stage are determined by incrementally increasing the debonding length d in mm until the total embedded length, is given in Equation (5) and Equation (6). The slip determined from the experiment during the debonding stage consists of the total slip from the elastic stage.

$$P_2 = \tau_{frc}\varphi d + \frac{\tau_{max}\varphi}{\beta}\tanh(\beta(L-d)) \tag{5}$$

$$S_{stage2} = S_1 + \frac{P_2 Q'}{\beta \sinh(\beta(L-d))}[\cosh(\beta(L-d)) - 1] + \frac{Q'd}{2}\left(\tau_{frc}\varphi d + 2P_2\right) \tag{6}$$

However, when the textile and the concrete are debonding completely, the slip due to the pullout force acts like a rigid body movement and the shear stress distribution is due to the dynamic bond strength (τ_{dyn}) in MPa. The limiting slip S_2 corresponding to the fully debonding condition is calculated from the experimental data and is taken into consideration to predict the slip in the dynamic stage 3. The pullout force in stage 3 and the total slip are calculated by incrementally providing a rigid body slip (Δ_d) in mm until the maximum embedded length. Equation (7) and Equation (8) predict the force and the slip during stage 3.

$$P_3 = \tau_{dyn}\varphi(L - \Delta_d) \tag{7}$$

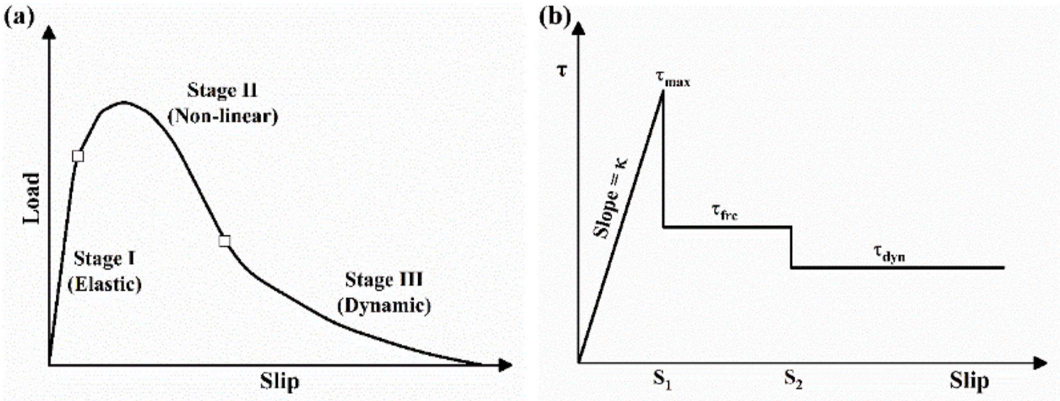

Fig. 12. (a) Typical pullout-slip behaviour; (b) Typical shear stress distribution.

$$S_{stage3} = S_2 + \Delta_d - \frac{\tau_{dyn}\varphi Q'}{2}(L - \Delta_d)^2 + P_3 Q'(L - \Delta_d) \quad (8)$$

5.2. *Comparison of the predicted pullout-slip behaviour*

The experimental data of all the samples for the pullout load test of each specimen were selected and the average load vs slip behaviour was calculated. The material properties of the textile reinforcement as given in Table 2 were adopted for predicting the pullout behaviour. Further, the properties (i.e., compressive strength and elastic modulus) of the high-performance 3D printable concrete were evaluated experimentally. The compressive strength and elastic modulus of control mix are 119 MPa and 58400 MPa respectively. However, the interface elastic modulus of 3D printable concrete depends on multiple factors like layer stiffness and thickness and printing parameters. Further, the elastic modulus of the control mix was considered for all the mixes as the compressive strength of all the mixes was observed to be similar.

Using Equation (4), the slip due to the incremental increase of load during the elastic stage was calculated. The predicted slip was observed to overestimate the stiffness of the specimens due to the assumption that all the filaments of the textile are fully bonded to the concrete. However, previous observations and SEM images show that not all the filaments of the multifilament yarns are bonded to the concrete [62,63] and also the strain distribution at the interface is not uniform. Unlike conventional concrete, penetration of 3D-printed concrete to the inner core filaments of the textile yarns is lesser and thus results in higher slip during the initial elastic phase of the pullout [35]. Hence, based on the comparison between the experimental results and the predicted values, a stiffness correction factor was calculated. The stiffness correction factor (α) was calculated for each specimen type by minimising the root mean square error between the experimental and predicted slip in stage 1. Further, while comparing the stiffness correction factor based on the rheological parameters (ratio of dynamic yield strength to plastic viscosity), a step behaviour was observed as shown in Fig. 13(a) (a similar behaviour was observed for all types of textiles).

It can be observed from the correlation that, as the mix becomes flowable (which shows the lower ratio of dynamic yield strength to

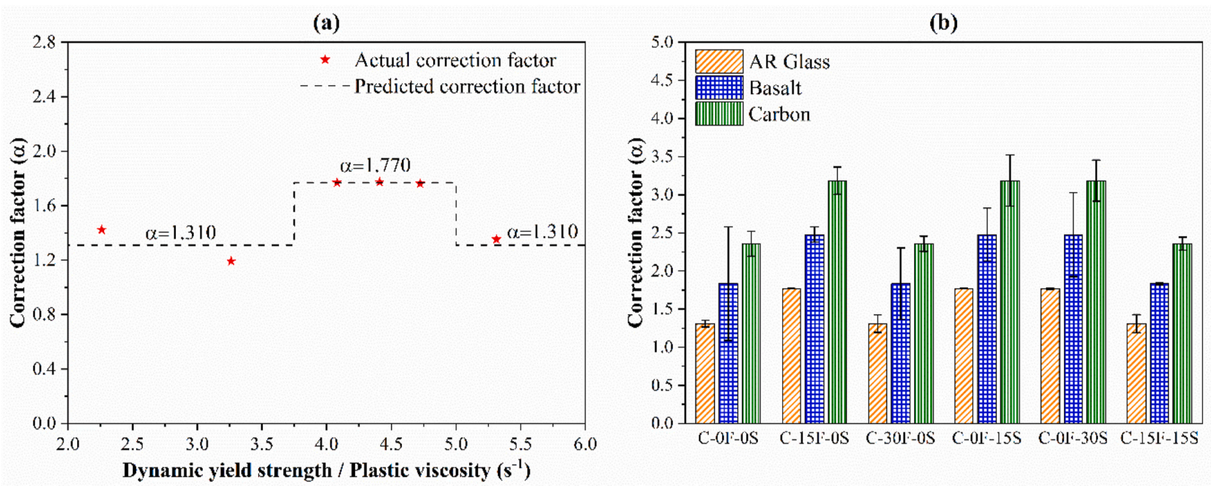

Fig. 13. (a) Correlating correction factor to the ratio of dynamic yield strength to plastic viscosity (the values are for AR-glass textile); (b) Correction factor for different textiles and mix proportions (error bar indicated the difference between actual α and predicted α).

plastic viscosity) the concrete penetrates better with the textile and the stiffness correction factor will be low. However, as the dynamic yield strength increases, the concrete tends to penetrate less to the filaments resulting in higher values of the correction factor. A similar trend was not observed for very high dynamic yield strength which needs further investigation. In addition, the correction factor for basalt and carbon textile specimens was observed to show a factored relationship to the correction factor of AR-glass textile for all the mix proportions. The values of the correction factor are represented by Equation (9) and Equation (10).

$$\alpha_{ARG} = \begin{cases} 1.310 & for\ 2.00 \le x < 3.75 \\ 1.770 & for\ 3.75 \le x \le 5.00 \\ 1.310 & for\ \ x > 5.00 \end{cases} \tag{9}$$

$$\alpha_{basalt} = 1.4\alpha_{ARG}\ ;\ \alpha_{carbon} = 1.8\alpha_{ARG} \tag{10}$$

Fig. 13(b) shows the correction factor for each type of textile for different mix proportions and the error bar represents the difference between the predicted and actual correction factors for all the types of textiles and mix proportions.

Further, based on the correction factor, modified stiffness $Q_c = \alpha Q^{'}$ was used in Equation (4) to Equation (8) instead of $Q^{'}$ and β was also calculated accordingly. The predicted pullout vs slip behaviour and the experimental pullout response were compared and are shown in Figs. 14–19.

The pullout behaviour predicted using the modified correction factor was observed to be comparable to the average response from the experimental results. Further trials with different mix proportions and variable embedded lengths need to be evaluated to formulate a more refined relation between the correction factor and the rheological parameters of 3D printable concrete. However, using the modified equations, the pullout response for the 3D-printed members can be predicted with accuracy.

6. Conclusions

The effect of rheological properties on the bond behaviour of textile-reinforced 3D printed concrete was evaluated in this study by varying the percentage replacement of fly ash and slag. The rheological parameters for different mix proportions measured using a rotational rheometer were reported. Further, to evaluate the bond behaviour between the matrix and the textile reinforcement, pull-out tests were performed and the parameters were analysed. To validate the nozzle efficiency and the bond between the textile and printable concrete, SEM micrographs were presented. Further, analytical equations were adopted to predict the pullout behaviour. Based on the test results from this study, the following conclusions were derived:

- The incorporation of fly ash and slag as a replacement for OPC for the 3D printable concrete mix was found to decrease the initial viscosity and dynamic yield strength of the control mix. The mixes with C-15F-0S and C-30F-0S demonstrated superior flowability when compared to the control mix, owing to their lower viscosity and dynamic yield strength. However, the addition of slag did not result in a significant reduction in the viscosity and dynamic yield strength.
- Furthermore, analysis of static yield strength development over time indicated that the inclusion of fly ash in the control mix resulted in decreased static yield strength development, whereas the addition of slag showed a higher rate of increase in static yield strength. The C-0F-15S mixture rapidly increased static yield strength after a resting period of 10 min, showing good buildability with sufficient ease in pumping.
- Similarly, evaluating the bond parameters suggested, a lower viscosity mix showed enhanced bond strength and pull-out load. Further, the C-30F-0S mix showed the highest improvement in the bond strength of about 64 % whereas the C-0F-15S showed a 40 % increase in the bond strength for AR-glass textile when compared to the C-0F-0S mix. However, unlike the C-30F-0S mix, the C-0F-15S mix also showed enhanced buildability with ease in pumping. Hence the results showed that the C-0F-15S mix was observed to be the optimum choice based on both rheological parameters and bond behaviour.
- In addition, examination of the SEM micrographs indicated that before pull-out, the concrete matrix effectively penetrated the spaces between the filaments, thereby enhancing bond strength. Following the pull-out, significant damage to the basalt and carbon textiles was observed during the debonding phase. Moreover, the SEM micrographs proved the effectiveness of the modified nozzle in improving the bond between the textile and the printable concrete.

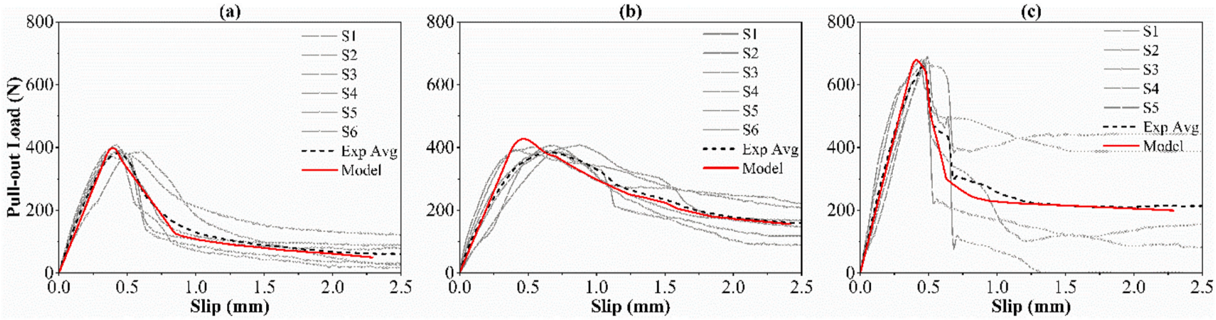

Fig. 14. Comparison of pullout behaviour of C-0F-0S (a) AR Glass (b) Basalt (c) Carbon.

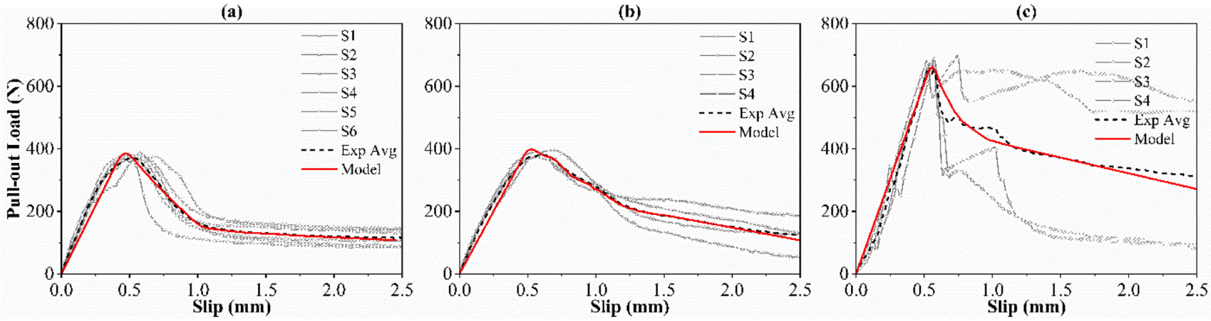

Fig. 15. Comparison of pullout behaviour of C-15F-0S (a) AR Glass (b) Basalt (c) Carbon.

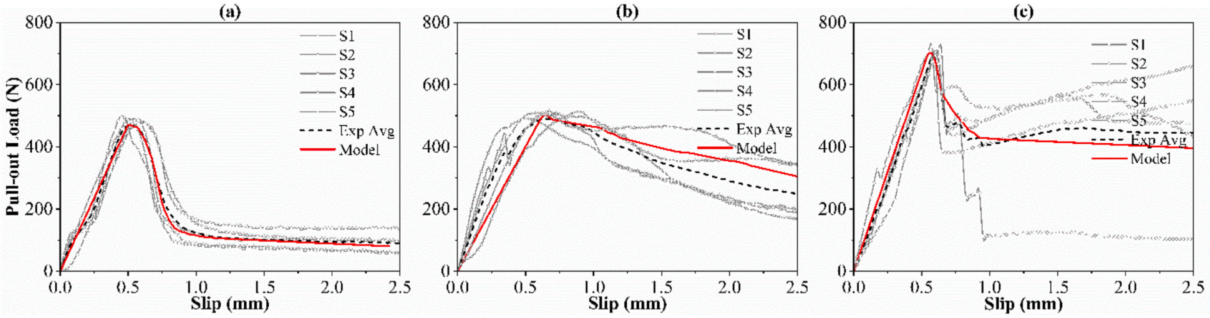

Fig. 16. Comparison of pullout behaviour of C-0F-15S (a) AR Glass (b) Basalt (c) Carbon.

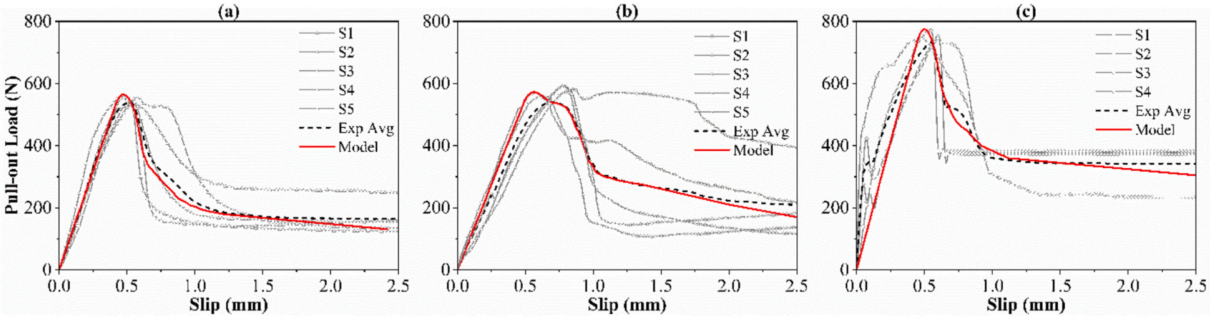

Fig. 17. Comparison of pullout behaviour of C-30F-0S (a) AR Glass (b) Basalt (c) Carbon.

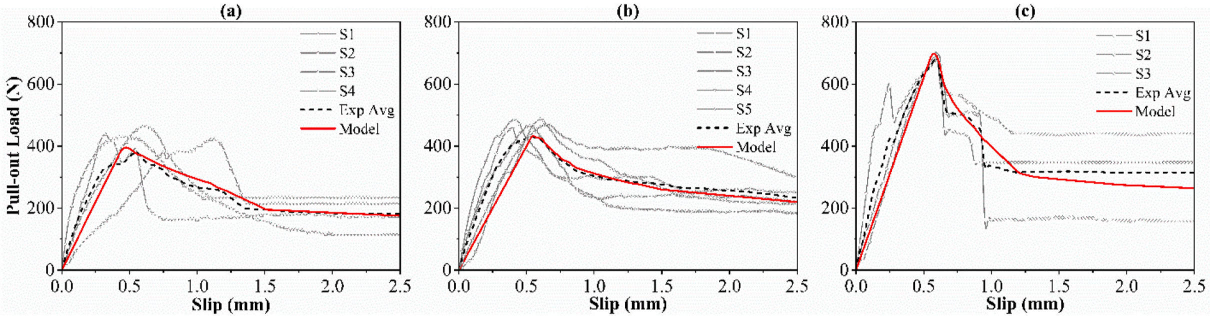

Fig. 18. Comparison of pullout behaviour of C-0F-30S (a) AR Glass (b) Basalt (c) Carbon.

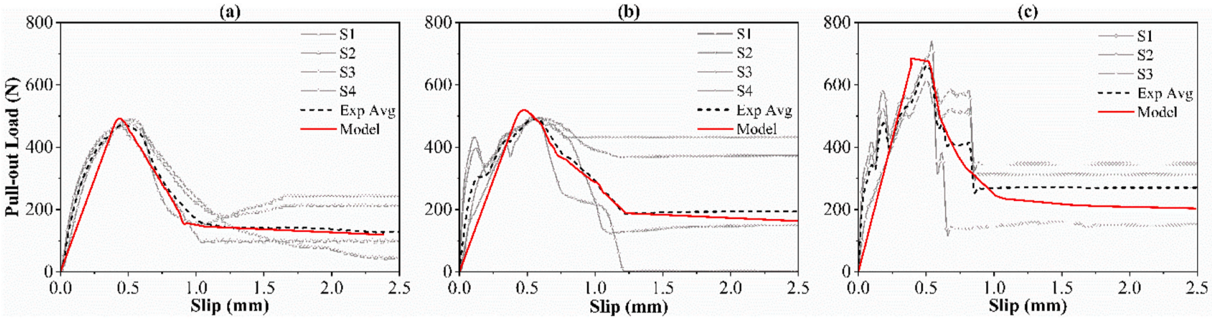

Fig. 19. Comparison of pullout behaviour of C-15F-15S (a) AR Glass (b) Basalt (c) Carbon.

- The predicted pullout-slip model was observed to show comparable results to the experimental data however, a correction factor needs to be introduced to accommodate the difference in the interface stiffness during the pull-out test. The correlation between the correction factor and the ratio between dynamic yield strength to plastic viscosity was derived. Further, between different types of textiles, a factored relationship between the correction factors can be observed and differences were observed to be minimal. Further trials to predict the relationship for the correction factor based on rheological properties can be considered in future studies to develop the pull-out bond-slip model.

The modified nozzle to incorporate textile reinforcement results in good bonding between the textile and printable mix. Moreover, by understanding the effect of rheological properties on the bond behaviour, it provides better understanding of the composite behaviour. This serves as a benchmark for the application of textile-reinforced 3D-printed concrete members in load bearing structures. Further, additional trials with varying rheological parameters needs to be conducted to predict the bond-slip behaviour of 3D-printed concrete and textile with better accuracy. In addition, the effect of embedment length and the pull-out bond slip behaviour on the composite action of textile-reinforced 3D-printed concrete members needs to be evaluated in detail. The adaptability of the modified nozzle facilitates the easy placement of textile along any desired print path, based on the geometry requirements of the structure. It also allows the placement of multiple layers of textile reinforcement and thus improves the structural performance. However, a more in depth investigation on providing automation systems to incorporate textile reinforcement for 3DCP applications and the structural behaviour of textile-reinforced 3D-printed concrete members needs to be evaluated.

CRediT authorship contribution statement

Akilesh Ramesh: Writing – original draft, Methodology, Investigation, Formal analysis, Data curation. **Pathmanathan Rajeev:** Writing – review & editing, Supervision, Resources, Methodology, Investigation, Formal analysis, Conceptualization. **Jay Sanjayan:** Writing – review & editing, Supervision, Methodology, Investigation, Formal analysis, Conceptualization.

Declaration of competing interest

Authors have no conflict of interest.

Data availability

Data will be made available on request.

Acknowledgement

The authors gratefully acknowledge the financial support from the Australian Research Council Grant DP210101680 and LE170100168 for the research work reported in this paper. Further, the authors acknowledge KAST GmbH company, Germany, for providing textile reinforcement. The authors are greatly thankful to the staff of the Digital Construction Laboratory at the Swinburne University of Technology.

References

[1] R.A. Buswell, et al., Freeform construction: mega-scale rapid manufacturing for construction, Autom. ConStruct. 16 (2) (2007) 224–231.
[2] W. Gao, et al., The status, challenges, and future of additive manufacturing in engineering, Comput. Aided Des. 69 (2015) 65–89.
[3] ASTM F2792-10: Standard Terminology for Additive Manufacturing Technologies, ASTM International, 2010.
[4] F. Bos, et al., Additive manufacturing of concrete in construction: potentials and challenges of 3D concrete printing, Virtual Phys. Prototyp. 11 (3) (2016) 209–225.
[5] R.A. Buswell, et al., 3D printing using concrete extrusion: a roadmap for research, Cement Concr. Res. 112 (2018) 37–49.
[6] D. Asprone, et al., Rethinking reinforcement for digital fabrication with concrete, Cement Concr. Res. 112 (2018) 111–121.
[7] T. Wangler, et al., Digital concrete: a review, Cement Concr. Res. 123 (2019) 105780.
[8] A. Perrot, D. Rangeard, A. Pierre, Structural built-up of cement-based materials used for 3D-printing extrusion techniques, Mater. Struct. 49 (2016) 1213–1220.
[9] A.R. Arunothayan, et al., Rheological characterization of ultra-high performance concrete for 3D printing, Cement Concr. Compos. 136 (2023) 104854.

[10] R. Jayathilakage, P. Rajeev, J. Sanjayan, Yield stress criteria to assess the buildability of 3D concrete printing, Construct. Build. Mater. 240 (2020) 117989.
[11] N. Roussel, Rheological requirements for printable concretes, Cement Concr. Res. 112 (2018) 76–85.
[12] J. Sanjayan, R. Jayathilakage, P. Rajeev, Vibration induced active rheology control for 3D concrete printing, Cement Concr. Res. 140 (2021) 106293.
[13] S. Muthukrishnan, S. Ramakrishnan, J. Sanjayan, Set on demand geopolymer using print head mixing for 3D concrete printing, Cement Concr. Compos. 128 (2022) 104451.
[14] S. Ramakrishnan, S. Kanagasuntharam, J. Sanjayan, In-line activation of cementitious materials for 3D concrete printing, Cement Concr. Compos. 131 (2022) 104598.
[15] J. Xiao, et al., Rheology of 3D printable concrete prepared by secondary mixing of ready-mix concrete, Cement Concr. Compos. 138 (2023) 104958.
[16] V.N. Nerella, S. Hempel, V. Mechtcherine, Effects of layer-interface properties on mechanical performance of concrete elements produced by extrusion-based 3D-printing, Construct. Build. Mater. 205 (2019) 586–601.
[17] F.P. Bos, et al., Experimental exploration of metal cable as reinforcement in 3D printed concrete, Materials 10 (11) (2017) 1314.
[18] T. Marchment, J. Sanjayan, Lap joint reinforcement for 3D concrete printing, J. Struct. Eng. 148 (6) (2022) 04022063.
[19] L. Pham, P. Tran, J. Sanjayan, Steel fibres reinforced 3D printed concrete: influence of fibre sizes on mechanical performance, Construct. Build. Mater. 250 (2020) 118785.
[20] C. Scott, Chinese Construction Company 3D Prints an Entire Two-Story House On-Site in 45 Days, 3dprint. com, 2016.
[21] T. Marchment, J. Sanjayan, Mesh reinforcing method for 3D concrete printing, Autom. ConStruct. 109 (2020) 102992.
[22] V.N. Nerella, H. Ogura, V. Mechtcherine, Incorporating reinforcement into digital concrete construction, in: Proceedings of IASS Annual Symposia, International Association for Shell and Spatial Structures (IASS), 2018.
[23] M. Hambach, M. Rutzen, D. Volkmer, Properties of 3D-printed fiber-reinforced Portland cement paste, in: 3D Concrete Printing Technology, Elsevier, 2019, pp. 73–113.
[24] A.R. Arunothayan, et al., Digital fabrication of eco-friendly ultra-high performance fiber-reinforced concrete, Cement Concr. Compos. 125 (2022) 104281.
[25] A.R. Arunothayan, et al., Fiber orientation effects on ultra-high performance concrete formed by 3D printing, Cement Concr. Res. 143 (2021) 106384.
[26] Z. Wu, A.M. Memari, J.P. Duarte, State of the art review of reinforcement strategies and technologies for 3D printing of concrete, Energies 15 (1) (2022) 360.
[27] C. Schröfl, V.N. Nerella, V. Mechtcherine, Capillary water intake by 3D-printed concrete visualised and quantified by neutron radiography, in: First RILEM International Conference on Concrete and Digital Fabrication–Digital Concrete 2018, Springer, 2019.
[28] A. Peled, A. Bentur, B. Mobasher, in: Textile Reinforced Concrete, 19, CRC Press, 2017.
[29] Y. Du, et al., Flexural behavior of basalt textile-reinforced concrete, Construct. Build. Mater. 183 (2018) 7–21.
[30] M. Halvaei, et al., Experimental investigation and modelling of flexural properties of carbon textile reinforced concrete, Construct. Build. Mater. 262 (2020) 120877.
[31] D.A. Bournas, et al., Textile-reinforced mortar versus fiber-reinforced polymer confinement in reinforced concrete columns, ACI Struct. J. 104 (6) (2007) 740.
[32] D.-Y. Yoo, et al., Comparative low-velocity impact response of textile-reinforced concrete and steel-fiber-reinforced concrete beams, J. Compos. Mater. 50 (17) (2016) 2421–2431.
[33] A. Volkova, et al., Flexural behavior of textile-reinforced concrete, in: MATEC Web of Conferences, EDP Sciences, 2016.
[34] S. Xu, et al., Bond characteristics of carbon, alkali resistant glass, and aramid textiles in mortar, J. Mater. Civ. Eng. 16 (4) (2004) 356–364.
[35] A. Peled, S. Sueki, B. Mobasher, Bonding in fabric–cement systems: effects of fabrication methods, Cement Concr. Res. 36 (9) (2006) 1661–1671.
[36] O. Boukendakdji, et al., Effect of slag on the rheology of fresh self-compacted concrete, Construct. Build. Mater. 23 (7) (2009) 2593–2598.
[37] H. Alghamdi, S.A. Nair, N. Neithalath, Insights into material design, extrusion rheology, and properties of 3D-printable alkali-activated fly ash-based binders, Mater. Des. 167 (2019) 107634.
[38] AS 3972 General Purpose and Blended Cements, Standards Australia, Sydney, Australia, 2010.
[39] AS 3582.3 Supplementary Cementitious Materials for Use with Portland and Blended Cement, Standards Australia, Sydney, Australia, 2016.
[40] AS 1478.1 Chemical Admixtures for Concrete, Mortar and Grout-admixtures for Concrete, Standards Australia, Sydney, Australia, 2000.
[41] Y. Liu, et al., Mechanical and fracture properties of ultra-high performance geopolymer concrete: effects of steel fiber and silica fume, Cement Concr. Compos. 112 (2020) 103665.
[42] P. Rajeev, et al., Using Fibre recovered from face mask waste to improve printability in 3D concrete printing, Cement Concr. Compos. 139 (2023) 105047.
[43] D. Feys, et al., Extension of the Reiner–Riwlin equation to determine modified Bingham parameters measured in coaxial cylinders rheometers, Mater. Struct. 46 (2013) 289–311.
[44] S. Muthukrishnan, S. Ramakrishnan, J. Sanjayan, In-line activation of geopolymer slurry for concrete 3D printing, Cement Concr. Res. 162 (2022) 107008.
[45] F.P. Bos, et al., Juxtaposing fresh material characterisation methods for buildability assessment of 3D printable cementitious mortars, Cement Concr. Compos. 120 (2021) 104024.
[46] J. Kruger, et al., 3D concrete printer parameter optimisation for high rate digital construction avoiding plastic collapse, Compos. B Eng. 183 (2020) 107660.
[47] D. Lootens, et al., Yield stress during setting of cement pastes from penetration tests, Cement Concr. Res. 39 (5) (2009) 401–408.
[48] O.H. Wallevik, et al., Avoiding inaccurate interpretations of rheological measurements for cement-based materials, Cement Concr. Res. 78 (2015) 100–109.
[49] J. Migunthanna, P. Rajeev, J. Sanjayan, Investigation of waste clay brick as partial replacement in geopolymer binder, Construct. Build. Mater. 365 (2023) 130107.
[50] S. Muthukrishnan, S. Ramakrishnan, J. Sanjayan, Effect of alkali reactions on the rheology of one-part 3D printable geopolymer concrete, Cement Concr. Compos. 116 (2021) 103899.
[51] J. Jiang, et al., Bond behavior of basalt textile meshes in ultra-high ductility cementitious composites, Compos. B Eng. 174 (2019) 107022.
[52] N. Trochoutsou, et al., Bond of flax textile-reinforced mortars to masonry, Construct. Build. Mater. 284 (2021) 122849.
[53] A. Nikravan, et al., Implementation of continuous textile fibers in 3D printable cementitious composite, in: International Symposium of the International Federation for Structural Concrete, Springer, 2023.
[54] J.J. van Rensburg, A.J. Babafemi, R. Combrinck, A textile reinforcement method for 3D printed concrete, in: MATEC Web of Conferences, EDP Sciences, 2022.
[55] B. Banholzer, Bond of a strand in a cementitious matrix, Mater. Struct. 39 (2006) 1015–1028.
[56] S. Venigalla, et al., Experimental and numerical simulation of pull-out response in textile-reinforced concrete, in: Structures, Elsevier, 2023.
[57] S. Sueki, et al., Pullout-slip response of fabrics embedded in a cement paste matrix, J. Mater. Civ. Eng. 19 (9) (2007) 718–727.
[58] A. Dalalbashi, B. Ghiassi, D.V. Oliveira, Textile-to-mortar bond behavior: an analytical study, Construct. Build. Mater. 282 (2021) 122639.
[59] M.T. Tran, X.H. Vu, E. Ferrier, Experimental and numerical investigation of carbon textile/cementitious matrix interfacebehaviourfrom pull-out tests, Construct. Build. Mater. 282 (2021) 122634.
[60] Y. Shao, C. Ouyang, S.P. Shah, Interface behavior in steel fiber/cement composites under tension, J. Eng. Mech. 124 (9) (1998) 1037–1044.
[61] S. Sueki, An Analytical and Experimental Study of Fabric-Reinforced, Cement-Based Laminated Composites, MS Thesis, Arizona State University, 2003.
[62] B. Banholzer, T. Brockmann, W. Brameshuber, Material and bonding characteristics for dimensioning and modelling of textile reinforced concrete (TRC) elements, Mater. Struct. 39 (2006) 749–763.
[63] B. Banholzer, Bond Behaviour of a Multi-Filament Yarn Embedded in a Cementitious Matrix, Bibliothek der RWTH Aachen, 2004.